

# A 3D Printed Bone Tissue Engineering Scaffold Composed of Alginate Dialdehyde-Gelatine Reinforced by Lysozyme Loaded Cerium Doped Mesoporous Silica-Calcia Nanoparticles

Mahshid Monavari, Rucha Medhekar, Qaisar Nawaz, Mehran Monavari, Miguel Fuentes-Chandía, Shahin Homaeigohar, and Aldo R. Boccaccini\*

A novel biomaterial comprising alginate dialdehyde-gelatine (ADA-GEL) hydrogel augmented by lysozyme loaded mesoporous cerium doped silica-calcia nanoparticles (Lys-Ce-MSNs) is 3D printed to create bioactive scaffolds. Lys-Ce-MSNs raise the mechanical stiffness of the hydrogel composite scaffold and induce surface apatite mineralization, when the scaffold is immersed in simulated body fluid (SBF). Moreover, the scaffolds can co-deliver bone healing (Ca and Si) and antioxidant ions (Ce), and Lys to achieve antibacterial (and potentially anticancer) properties. The nanocomposite hydrogel scaffolds can hold and deliver Lys steadily. Based on the *in vitro* results, the hydrogel nanocomposite containing Lys assured improved pre-osteoblast cell (MC3T3-E1) proliferation, adhesion, and differentiation, thanks to the biocompatibility of ADA-GEL, bioactivity of Ce-MSNs, and the stabilizing effect of Lys on the scaffold structure. On the other hand, the proliferation level of MG63 osteosarcoma cells decreased, likely due to the effect of Lys. Last but not least, cooperatively, alongside gentamicin (GEN), Lys brought about a proper antibacterial efficiency to the hydrogel nanocomposite scaffold against gram-positive and gram-negative bacteria. Taken together, ADA-GEL/Lys-Ce-MSN nanocomposite holds great promise for 3D printing of multifunctional hydrogel bone tissue engineering (BTE) scaffolds, able to induce bone regeneration, address infection, and potentially inhibit tumor formation and growth.

## 1. Introduction

Various medical scenarios such as tumor resection, trauma, deformities, among others, lead to the formation of bone defects. The treatment of bone defects and their reconstruction can be properly realized by developing flexible, customized, and bioactive scaffolds that match the damaged bone cavity physically and interact with the neighboring bone tissue biochemically.<sup>[1,2]</sup> In this regard, different biodegradable and even nondegradable formulations have been studied that can be shaped to fit the bone defect by advanced processing techniques such as 3D printing.<sup>[3,4]</sup> 3D printed BTE scaffolds efficiently imitate the natural microenvironment in terms of provision of a 3D architecture equipped with necessary biochemical cues for the attachment and proliferation of bone cells.<sup>[4-6]</sup> Hydrogels are widely investigated materials for 3D printing of BTE scaffolds. Hydrogels can properly recapitulate the conditions of the native extracellular matrix, thanks to their customizable degradation behaviour and functionality.<sup>[6]</sup> However, hydrogels are


M. Monavari, R. Medhekar, Q. Nawaz, M. Fuentes-Chandía, A. R. Boccaccini  
Institute of Biomaterials  
Department of Materials Science and Engineering  
University of Erlangen-Nuremberg  
91058 Erlangen, Germany  
E-mail: aldo.boccaccini@fau.de

R. Medhekar  
Institute of Biomaterials and Advanced Materials and Processes Master Programme  
University of Erlangen-Nuremberg  
91058 Erlangen, Germany

M. Monavari  
Section eScience (S.3)  
Federal Institute for Materials Research and Testing  
Unter den Eichen 87, 12205 Berlin, Germany

M. Fuentes-Chandía  
Department of Biology  
Skeletal Research Center  
Case Western Reserve University  
Cleveland, Ohio 44106-7080, USA

S. Homaeigohar  
School of Science and Engineering  
University of Dundee  
Dundee DD1 4HN, United Kingdom

 The ORCID identification number(s) for the author(s) of this article can be found under <https://doi.org/10.1002/mabi.202200113>

© 2022 The Authors. Macromolecular Bioscience published by Wiley-VCH GmbH. This is an open access article under the terms of the Creative Commons Attribution License, which permits use, distribution and reproduction in any medium, provided the original work is properly cited.

DOI: 10.1002/mabi.202200113

mechanically weak and rarely bioactive, thus pose significant challenges with respect to BTE wherein robust, cell-interactive scaffolds play a pivotal role.<sup>[1,7]</sup> One successful strategy put forward to address the mentioned bottlenecks is the hybridization of hydrogels by adding inorganic fillers including bioactive glass (BG) nanoparticles.<sup>[3,8,9]</sup> For instance, Zhu et al.<sup>[10]</sup> have reported that BG/sodium alginate hydrogel can offer an anti-inflammatory effect via polarizing macrophages toward M2 phenotype both in cell culture tests and in animal models. In another relevant study,<sup>[11]</sup> it has been proven that copper doped BG incorporated in furan-sodium alginate/bis-maleimide-polyethylene glycol induces bone regeneration through the release of osteogenic and angiogenic ions such as Ca, Si, and Cu.

Natural polymer-based hydrogels such as gelatine and alginate are widely studied for a plethora of biomedical applications.<sup>[12–15]</sup> Gelatine-made hydrogels are biocompatible and highly degradable. They also encompass the Arginine-Glycine-Aspartic acid (RGD) peptide sequence that facilitates cell adhesion.<sup>[16]</sup> Despite such merits, gelatine hydrogels are mechanically weak.<sup>[17]</sup> On the other hand, alginate hydrogels show poor cell adhesion mainly due to the absence of cell-binding moieties.<sup>[18,19]</sup> As a promising solution, partially oxidizing alginate and its combination with gelatine to form alginate dialdehyde-gelatine (ADA-GEL) hydrogels have been developed to address the respective shortcomings of each constituent.<sup>[20]</sup> ADA-GEL is a cell (e.g., fibroblast<sup>[21]</sup> and osteoblasts<sup>[22]</sup>) supportive and durable hydrogel with promising potential in BTE<sup>[3]</sup> and in construction of 3D tumour models.<sup>[23]</sup> The combination of ADA-GEL with BG nanoparticles has been also investigated by a number of research groups. For example, Leite et al.<sup>[8]</sup> created 3D-printed ADA-GEL nanocomposite constructs including BG nanoparticles that could drive the synthesis of a bone-mimicking apatite layer on the surface when submerged in simulated body fluid (SBF). Sarker et al.<sup>[24]</sup> demonstrated that ADA-GEL scaffolds incorporating silicate BG nanoparticles are mechanically stronger than the pristine ADA-GEL scaffold and enable more optimum cell-material interactions. Rottensteiner et al.<sup>[9]</sup> proved that inclusion of BG nanoparticles (45S5 BG composition) into ADA-GEL could provoke adhesion, proliferation, and growth of bone marrow-derived mesenchymal stem cells (MSCs) seeded on the surface of the composite.

Compared to dense BG nanoparticles, mesoporous BG nanoparticles (MSNs) feature a much larger specific surface area and an adjustable pore size in the nanoscale,<sup>[25,26]</sup> thus allowing for co-delivery of beneficial ions and biological agents<sup>[26,27]</sup> with different therapeutic effects. In this regard, we recently reported the reinforcement of ADA-GEL hydrogel using icariin-loaded (SiO<sub>2</sub>-CaO) MSNs to create 3D printed BTE scaffolds.<sup>[3]</sup> In the current study, to extend the applicability of such a nanocomposite hydrogel in BTE, MSNs are upgraded via cerium (Ce) doping to acquire an antioxidant effect, which is crucial for alleviation of the oxidative stress level associated with bone remodeling and bone diseases.<sup>[28]</sup> Additionally, Lys is loaded on MSNs to endow the nanocomposite hydrogel with antibacterial<sup>[29]</sup> and anticancer<sup>[30]</sup> properties. Lys is an enzyme able to induce lysis of bacteria via hydrolysis of specific peptidoglycan bonds available in the cell wall.<sup>[29]</sup> The enzyme also contributes to the performance of the human innate immune system<sup>[18]</sup> and can hinder tumor formation and growth.<sup>[30]</sup> Consequently, codelivery of Ce

and Lys by the 3D printed Lys-Ce doped MSNs incorporated ADA-GEL (ADA-GEL/Lys-Ce-MSN) scaffold is expected to induce antioxidant, antibacterial, anticancer, and pro-angiogenesis effects, beneficial for bone regeneration. As the second class of such nanocomposite hydrogels, Gentamicin, an aminoglycoside antibiotic that properly inactivates gram-negative bacteria,<sup>[31]</sup> will also be included in the nanocomposite hydrogel to further support antibacterial activity. Commonly, gentamicin is prescribed with other antibiotics such as  $\beta$ -Lactams with a gram-positive antibacterial effect to induce a synergistic, broad spectrum bactericidal activity.<sup>[32]</sup> Given that Lys is well-known as a gram-positive antibacterial factor,<sup>[33,34]</sup> gentamicin was co-loaded to assure the creation of a nanocomposite scaffold with a broad-spectrum antibacterial activity.

## 2. Experimental Section

### 2.1. Materials

Aqueous ammonia (1 M), cetrimonium bromide (CTAB), tetraethyl orthosilicate (TEOS), ethyl acetate (EA), ethanol (96%), calcium nitrate tetrahydrate (CaN), and cerium (III) nitrate hexahydrate were obtained from Sigma-Aldrich (Darmstadt, Germany) and used as received. Ultrapure water was prepared by using Milli-Q equipment (Millipore, Billerica, MA, USA). Dulbecco's phosphate-buffered saline (DPBS, pH  $\approx$ 7.4) and Dulbecco's modified Eagle's medium (DMEM) were purchased from Gibco® (Darmstadt, Germany). Fetal bovine serum (FBS), penicillin, streptomycin, l-glutamine (Gibco®, Darmstadt, Germany), and dimethylsulphoxide (DMSO) were purchased from Thermo Fisher Scientific (Waltham, USA). Lysozyme (Lys,) and Gentamicin (Gen) were also obtained from Sigma-Aldrich and Gibco®, respectively. The bacteria strains of *Escherichia coli* (*E. coli*, ATCC25922) and *Staphylococcus aureus* (*S. aureus*, ATCC25923) were purchased from the Leibniz Institute DSMZ-German Collection of Microorganisms and Cell Cultures (Braunschweig, Germany). Lysogeny broth (LB) medium and Luria-Bertani agar were obtained from Carl Roth GmbH (Karlruhe, Germany).

### 2.2. Synthesis of MSNs

MSNs were synthesized via a microemulsion-assisted sol-gel method following the protocol described in the literature.<sup>[35]</sup> As shown in **Figure 1a**, CTAB (0.7 g), EA (10 ml), aqueous ammonia (1 M; 7 ml), TEOS (3.6 ml), and CaN (2.28 g) were one by one dissolved in deionized water (33 ml) and the solutions prepared at each step were stirred at 35 °C for a given time depending on solubility of the added material. The as-prepared solution was ultimately centrifuged to separate the synthesized nanoparticles, which were subsequently washed two times using deionized water and one time using ethanol. The nanoparticles were last dried overnight at 6 °C and then calcined for 3 h at 700 °C in a furnace with a heating rate of 2 °C min<sup>-1</sup> under an air atmosphere.

### 2.3. Cerium Doping of MSNs

The synthesized MSNs were doped with Ce (Ce-MSNs), following a previously reported protocol.<sup>[36,37]</sup> To do so, MSNs were sus-

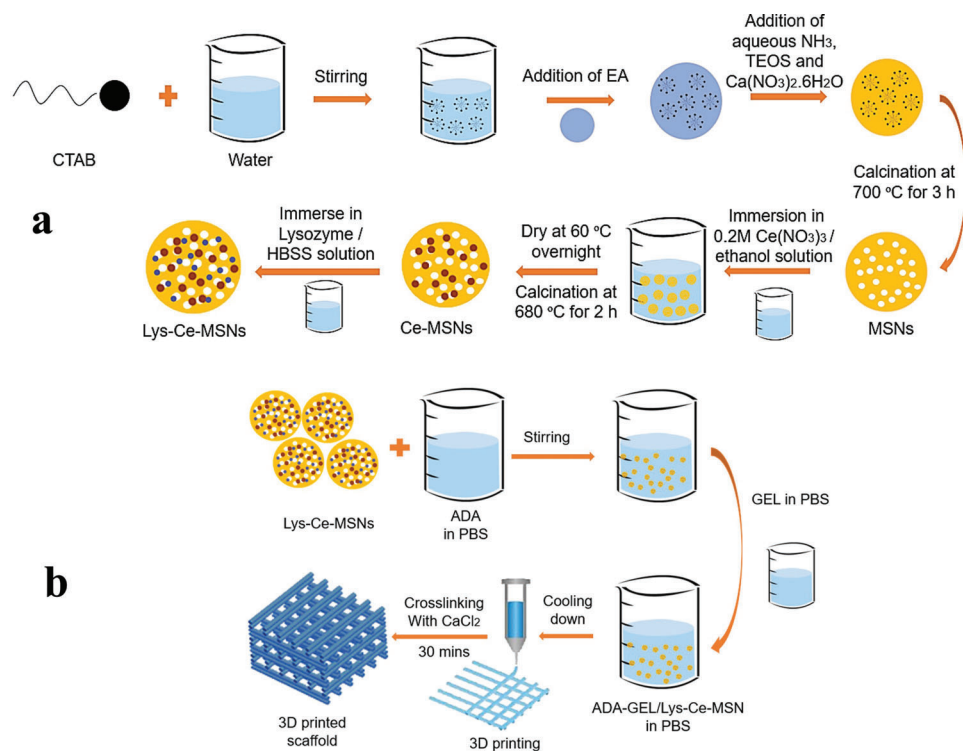


**Figure 1.** Schematic demonstration of the synthesis procedure of Lys-Ce-MSNs a) and 3D printed ADA-GEL/Lys-Ce-MSN scaffolds b).

pendent in a cerium nitrate-ethanol solution (0.2 M) under continuous stirring for 24 h at room temperature. At this step, 60 ml of the cerium nitrate solution was used per each gram of MSNs. The as-treated MSNs were later collected by centrifuging the suspension and washed twice with ethanol. Subsequently, Ce-MSNs were dried at 60 °C overnight and later calcined in a furnace at 680 °C for 2 h with a heating rate of 2 °C min<sup>-1</sup> to exclude the residual nitrate and to stabilize the structure. The preparation procedure of Ce-MSNs is schematically illustrated in Figure 1a.

## 2.4. Physicochemical Characterization

The morphology of Ce-MSNs and nanocomposite hydrogel scaffolds was observed using a field emission scanning electron microscope (FESEM) (Auriga, Zeiss, Germany). For this purpose, the nanoparticles/ethanol dispersion was homogenized by ultrasonication and later dropwise deposited on electrically conductive aluminum tapes and later sputter-coated with a thin Au layer. With respect to the scaffolds, they were first fixed by immersing them in the SEM fixing solutions I and II (mixture of glutaraldehyde-formaldehyde in water with or without sucrose) for 30 min each. Afterward, they were immersed in an ethanol series (30%, 50%, 70%, 80%, 90%, 95%, and 99%) for 30 min at each concentration to get dehydrated and eventually dried within a critical point dryer (Leica EM CPD300, Germany). To analyze the elemental composition of the samples (Ce-MSNs and scaffold surface), energy dispersive spectroscopy (EDS, X-MaxN Oxford Instruments, UK) was carried out at the applied voltage of 20 kV and considering a 6 mm working distance during SEM measure-

ment. Last, the samples' surface chemistry was investigated by using ATR-FTIR (IR-Affinity-1S, Shimadzu, Japan). ATR-FTIR spectroscopy was performed at the resolution of 4 cm<sup>-1</sup> and by applying 40 scans within the wavenumber range of 400 to 2000 cm<sup>-1</sup>.

## 2.5. Lysozyme Loading and Release from Ce-MSNs

The Lys loading efficiency of Ce-MSNs was determined by immersing 100 mg of the nanoparticles in Lys/HBSS (Hank's Balanced Salt Solution) solutions of varying concentrations (600, 800, and 1000 µg ml<sup>-1</sup>) for 20, 30, and 60 min. The as-prepared suspensions were then centrifuged and supernatants were analyzed in terms of Lys concentration. The amount of the unloaded Lys present in HBSS was quantified by using a UV-vis spectrophotometer (Specord 40, Analytik Jena AG) at the enzyme's characteristic wavelength ( $\lambda = 282$  nm) via correlating the absorbed light intensity to enzyme concentration based on a pre-constructed calibration graph.

The Lys release behavior from Ce-MSNs was quantified after immersion of 100 mg of Lys-Ce-MSNs in 20 mL of HBSS and placement of the suspensions in a shaking incubator (KS 4000i control, IKA, Germany) for 21 days at physiological temperature. At given time intervals, after centrifugation, 1 ml of the supernatant was removed and the suspensions were replenished with 1 mL of fresh HBSS. The removed supernatants were examined in terms of Lys concentration using the above-mentioned UV-vis spectrophotometer.

## 2.6. 3D Printing of ADA-GEL/Ce-MSN Scaffolds

The inks for 3D printing were formulated based on dissolving 7.5% GEL and 5% ADA in phosphate-buffered saline (PBS) and dispersing 0.1% of Ce-MSNs with and without Lys in the resulting solution. ADA was first dissolved in half of the whole PBS volume and the solution was stirred at room temperature overnight. MSNs were then added to the solution and stirred until they became homogeneously distributed. GEL was dissolved in the remaining amount of PBS and the solution and suspension were then mixed and stirred at 37 °C for 10 min. In the case of Gen containing hydrogel scaffolds, Gen (50 µg ml<sup>-1</sup>) was added to the ADA-GEL/(Lys)Ce-MSN suspension. The mixture suspension was subsequently poured into a cartridge, which was later cooled down in a fridge for 10 min to allow its gelation. The cartridge containing the ADA-GEL/(Lys)Ce-MSN hydrogel was loaded on a pneumatic 3D printer (BioScaffolder 3.1 GeSim printer). The printing parameters such as pressure, printing speed, and scaffold dimensions were optimized to create open porous grid-like square shaped (15 mm in length) scaffolds. The scaffolds were 3D printed in four layers along the z-axis with 10 struts over the length. The pore circularity and printability of the scaffolds were determined based on pore area using the following equations (1 and 2)<sup>[38]</sup>:

$$\text{Circularity of pores (C)} = 4\pi \times P \text{ area} \quad (1)$$

$$\text{Printability (P)} = \pi / (4C) \quad (2)$$

Eventually, the 3D printed scaffolds were immersed in a CaCl<sub>2</sub> aqueous solution (0.2 M) for 30 min to be cross-linked. The preparation procedure of the 3D printed ADA-GEL/Lys-Ce-MSN scaffolds is schematically shown in Figure 1b.

## 2.7. Mechanical Testing of ADA-GEL/Ce-MSN Scaffolds

To determine the mechanical properties of the 3D printed scaffolds after inclusion of Ce-MSNs, a compression test was performed. In this study, using a puncher, round-shaped discs (3 mm in diameter and 2 mm in height) were fabricated. The compressive stiffness of the hydrogel scaffolds was determined using a Microtester (Cellscale, Canada) applying a compression displacement of 15%.

## 2.8. Lys and GEL Release and Degradation Behavior of ADA-GEL/Lys-Ce-MSN Scaffolds

The 3D printed scaffolds composed of ADA-GEL/Ce-MSN with or without Lys were immersed in HBSS containing beakers located inside a shaking incubator (80 rpm) for 21 days at physiological temperature. At given intervals, 1 ml of the supernatant was taken and instead an equal amount of fresh HBSS was added. The cumulative release of Lys was quantified by UV-vis spectroscopy considering a pre-constructed calibration graph. The GEL release was investigated via the Biuret colorimetric test. In this test, the Biuret reagent (Sigma, USA) was employed for identification of the peptide bonds that drive the reduction of Cu<sup>2+</sup>

ion to Cu<sup>+</sup> ion in an alkaline solution, thereby forming a purple-colored compound. This measurement was carried out by taking the sample solution (0.1 ml) and mixing it with the Biuret reagent (1.1 ml) for 10 min at room temperature. Afterward, the Folin and Ciocalteu's phenol Reagent (FCR) (50 µl) was added to the solution and the new solution remained to react for 30 min. The generated color's intensity (as quantified by UV-vis spectroscopy (λ = 758 nm)) was correlated to the quantity of the released GEL via a pre-constructed calibration graph. The release of ions and GEL from the scaffolds alters the medium pH. Thus, the pH level can represent the degradation extent. The medium pH was determined using the same supernatants taken for the Lys release assay.

In vitro degradation tests were carried out through incubation of the 3D printed scaffolds immersed in 5 ml of supplemented alpha-minimum essential medium (α-MEM) within a shaking incubator (80 rpm) at physiological temperature for 28 days. The medium was refreshed every 2 days and at given intervals, the scaffolds were taken out from the medium and then weighed. The weight loss percentage of the scaffold (W<sub>r</sub>) was quantified via the following equation (3):

$$W_r = \left( \frac{W_t}{W_0} \right) \times 100 \quad (3)$$

where W<sub>0</sub> and W<sub>t</sub> represent the sample's initial and momentary weight, respectively.

## 2.9. Formation of Hydroxyapatite (HA) Surface Layer on ADA-GEL/Ce-MSN Scaffold

The formation of HA surface layer on the 3D printed scaffolds was studied under sterile conditions by immersing the samples in 20 ml of SBF for 21 days at 37 °C. At given time points, the scaffold was removed from SBF and the formation of HA was monitored by SEM, FTIR, EDS, and X-Ray Diffraction (XRD). The SBF was prepared according to the protocol of Kokubo et al.<sup>[39]</sup>.

## 2.10. Cell Culture Protocol

Human bone osteosarcoma cell line, MG63, was cultured in DMEM, supplemented with 10% (v/v) of FBS and 1.0% (v/v) penicillin-streptomycin. The undifferentiated pre-osteoblastic cell line MC3T3-E1 was cultured in supplemented α-MEM with extra 1.0% (v/v) L-Glutamine. The cell incubation conditions included: temperature of 37 °C and atmosphere of 5% CO<sub>2</sub> and 95% relative humidity. The cells were eventually passaged based on standard protocols. The cell experiments were carried out using 1 × 10<sup>5</sup> cells per well in 6-well plates.

## 2.11. Cell Proliferation

The cell proliferation was characterized by a colorimetric WST-8 bioassay (Sigma Aldrich, Germany). The experiment was carried out using three replicas of the samples (3D printed scaffolds) in

different compositions under sterile conditions. An equal density of the above mentioned cells was added to the scaffold containing wells and the cells were allowed to adhere onto the scaffold surface over the course of incubation, i.e., 7 days, at 37 °C and under 5% CO<sub>2</sub>. The culture medium was renewed once in 3 days. On the 2nd, 4th, and 7th days, 1 ml of WST-8 solution (5% v/v) was added to the wells and incubation continued for 3 h. The cell viability was measured by transfer 100 µl of the medium to a new (96) well plate and reading the optical absorbance (at λ = 450 nm) by a multi-mode microplate reader (CLARIOstar®plus, BMG Labtech, Germany).

### 2.12. Live-Dead Assay and Cell Adhesion Assay

The cell viability and cell distribution mode were visualized by Calcein-AM/Phalloidin/DAPI (Invitrogen, USA) staining and subsequent fluorescence microscopy imaging. SEM was also employed to image the cell morphology. Both imaging approaches were carried out after 40 h and 4 and 7 days of cell-scaffold incubation. To do so, the scaffolds were first rinsed using HBSS and then treated using a diluted calcein-AM/HBSS solution (4 µl ml<sup>-1</sup>) while being incubated for 45 min. Thereafter, the scaffolds were rinsed again using HBSS and the adhered cells were fixed by formaldehyde (3.8% (v/v)) for 15 min at ambient temperature. To stain the cell actin filaments, rhodamine-phalloidin (8 µl ml<sup>-1</sup> HBSS) was added to the scaffolds after cell fixation, and the assembly was left for 1 h in an incubator. The nuclei were stained with DAPI (1 µl ml<sup>-1</sup> HBSS) in 5 min after they were washed with HBSS. Finally, the images of the stained cells were captured via fluorescence microscopy and were merged by using the ImageJ software.

### 2.13. Alkaline Phosphatase (ALP) Analysis

To analyze the osteogenic behavior of the scaffolds, ALP activity was photometrically measured after 7 and 14 cell culture days. Briefly, at the mentioned time points, MC3T3-E1 cells were properly lysed by a lysis buffer (at pH 7.5) containing 10 × 10<sup>-3</sup> M Tris-HCl, 0.05% Triton X-100 (pH 10.0), and 1 × 10<sup>-3</sup> M MgCl<sub>2</sub>. The ALP activity was measured by 4-p-nitrophenyl phosphate (0.1 × 10<sup>-3</sup> M) that was enzymatically dissociated by ALP. NaOH solution (650 µl, 1 M) was employed to stop the process after 30 min incubation at room temperature. Thereafter, optical absorbance was measured at λ = 405 and 690 nm by a Specord 40 UV-vis spectrophotometer (Analytik Jena AG, Germany). The ALP induced conversion extent of para-nitrophenyl phosphate (pNPP) to para-nitrophenol (pNP) over time (per minute) indicated ALP activity that was later normalized to the total protein content to measure the specific ALP activity. The Bradford test was employed to measure the cells' total protein content. To do so, the lysed cells supernatant (25 µL) was transferred to a cuvette containing the Bradford protein assay kit (AppliChem GmbH, Germany) (975 µL). The optical absorbance intensity of the as-prepared solution kept in the dark was determined at λ = 595 nm via UV-vis spectrophotometry after 10 min.

### 2.14. Mineralization Assay

Cell induced HA deposition on the scaffolds was monitored using the OsteoImage® fluorescent staining kit (Lonza). The fluorescent staining of HA was carried out on the 14th and 21st days of cell culture on the scaffolds according to the protocol introduced by the manufacturer. To do so, the scaffolds were first thoroughly rinsed using HBSS and thereafter fixed for 20 min using a 3.7% (v/v) paraformaldehyde solution including a fixing buffer. Afterward, the scaffolds were rinsed twice using a diluted (10×) OsteoImage wash buffer and subsequently stained with a diluted (1:100) OsteoImage staining reagent, followed by incubation for 0.5 h. The staining reagent was later discarded and the scaffolds were rinsed thrice using a diluted wash buffer. Eventually, the images were captured by a fluorescence microscope. The quantitative assay was performed by using a multi-mode microplate reader (CLARIOstar®plus, BMG Labtech, Germany) at the excitation/emission dual wavelengths of 492/520 nm.

### 2.15. Antibacterial Test

The antibacterial activity of the 3D-printed scaffolds containing Lys and Gen was characterized against *S. aureus* (gram-positive) and *E. coli* (gram-negative) bacteria via the agar-plate assay and turbidity assay. For the first assessment, 20 ml of the agar medium was poured into a Petri plate and cooled to be solidified. The plate was later inoculated with 15 µl of inoculum that was spread uniformly on the solidified agar medium. The 3D printed ADA-GEL/Ce-MSN and ADA-GEL/Lys-Ce-MSN scaffolds with or without Gen were mounted on the agar plates and then incubated for 24 h at 37 °C to form respective inhibition zones. Regarding the turbidity assay, first, the bacteria strains were incubated in the LB medium for 24 h at 37 °C under shaking conditions to gain the logarithmic phase of growth. Subsequently, optical density (OD) of the bacteria colony was calibrated at λ ≈ 600 nm (Thermo Scientific™ GENESYS 30™, Germany) to reach 0.015, according to the standard protocol for measurement of the turbidity of bacterial cultures. Each sterilized scaffold was placed in one well of a 12-well plate containing 2 ml of the LB medium plus 15 µl of the bacteria suspension and then incubated for 48 h at 37 °C. Afterwards, 100 µl of the medium from each sample containing well was shifted to a 96-well plate. The bacteria suspension in the LB medium and the LB medium were employed as the control and blank samples, respectively. Finally, the samples' OD values were quantified at λ ≈ 600 nm and thereby bacterial viability was determined as follows (equation 4)<sup>[40]</sup>:

$$\text{Bacterial viability (\%)} = \left( \frac{\text{OD sample} - \text{OD Blank}}{\text{OD control} - \text{OD Blank}} \right) \times 100 \quad (4)$$

### 2.16. Statistical Analysis

The obtained biological data were statistically analyzed through the one-way analysis of variance (ANOVA) method. The *p*-values < 0.05 indicated a meaningful (significant) discrepancy between the compared data.

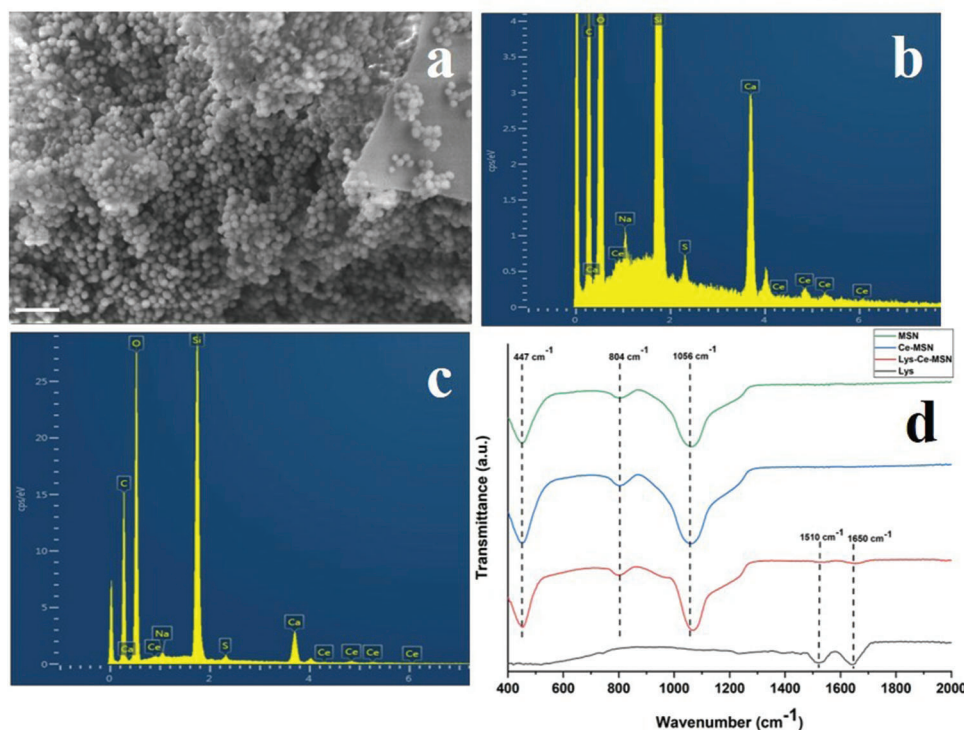


**Figure 2.** a) SEM image showing the morphology and size distribution of Lys-Ce-MSNs (the scale bar represents 1  $\mu\text{m}$ ). EDS spectra verifying the coexistence of Ca, Ce, and Si, in: b) Ce-MSNs and c) Lys-Ce-MSNs. d) ATR-FTIR spectra representing the surface chemistry of MSNs doped with Ce and loaded with Lys.

### 3. Results and Discussion

#### 3.1. Physicochemical Properties of Lys-Ce-MSNs

As shown in **Figure 2a**, Lys-Ce-MSNs are spherical and almost monodisperse in terms of particle size ( $\approx 100\text{--}200$  nm determined by using the ImageJ software). A few ellipsoidal particles also formed thanks to the firm adhesion of the microemulsion templating droplets during the synthesis.<sup>[28]</sup> The obtained particle size matches well with the values already reported for MSNs similarly synthesized through microemulsion-based techniques.<sup>[28,35,37]</sup> The EDS analysis, **Figure 2b,c**, verifies the presence of Ca, Si, and Ce in both groups of nanoparticles, though with lower peak intensities that could be related to the surface coverage of the nanoparticles with a Lys coating. **Figure 2d** shows the ATR-FTIR spectra for all classes of nanoparticles including MSNs, Ce-MSNs, and Lys-Ce-MSNs as well as Lys as a control. Commonly, all MSNs possess the characteristic band of Si–O–Si appearing at  $447\text{ cm}^{-1}$  (rocking mode),  $804\text{ cm}^{-1}$  (bending mode), and  $1056\text{ cm}^{-1}$  (stretching mode).<sup>[41]</sup> Additionally, ATR-FTIR spectra for Lys-Ce-MSNs and Lys feature two dips at  $1510$  and  $1650\text{ cm}^{-1}$  that are absent for the enzyme-free nanoparticles and are assigned to the characteristic amide (I and II) bands of Lys.<sup>[42]</sup> Such dips are highly faded in the case of Lys-Ce-MSNs, most likely owing to formation of a covalent (coordinate) bond between Lys (electron-donating amide groups) and the nanoparticles' metal ions and emergence of metal-protein complexes. Such an interaction potentially affects the secondary structure (conformation mode) of the enzyme and disintegrates the long chain

of the polypeptide, reflected in the low dip intensity of amide bands in Lys-Ce-MSNs.<sup>[43]</sup> With respect to the Lys loading mechanism, other than likely formation of a covalent bond between Lys and Ce-MSNs, electrostatic interaction and hydrogen bonding can also play a role. Knowing that silica nanoparticles' isoelectric point is  $\approx 2$ ,<sup>[44]</sup> MSNs possess a highly negatively charged surface, thereby electrostatically attracting the positively charged (protonated) Lys molecules with isoelectric point of 11.<sup>[45]</sup> The electrostatic interaction between Lys and mesoporous bioactive glass has been also reported by Lou et al.<sup>[46]</sup> Particularly, hydrogen bonding between the amide groups of Lys and surface hydroxyl groups of Ce-MSNs is plausible.

#### 3.2. Lys Loading/Release Behavior of Ce-MSNs

The Lys loading efficiency of Ce-MSNs over different time periods (at the Lys concentration of  $1\text{ mg ml}^{-1}$ ) is demonstrated in **Figure 3a**. As seen in this figure, after 20 min, loading efficiency reaches a plateau and MSNs are fully saturated with Lys. To characterize the optimum Lys concentration, Ce-MSNs were immersed in Lys/HBSS solutions with different Lys concentrations. As shown in **Figure 3b**, both Lys concentrations of  $600$  and  $800\text{ }\mu\text{g ml}^{-1}$  provide high loading efficiencies of 93% and 90%, respectively. Taking into consideration the therapeutic window of Lys,<sup>[47]</sup>  $800\text{ }\mu\text{g ml}^{-1}$  was selected as the optimum concentration for the synthesis of Lys-Ce-MSNs in this study.

With respect to the enzyme release, as seen in **Figure 3c**, the Lys delivery by Lys-Ce-MSNs follows an ascending trend until the

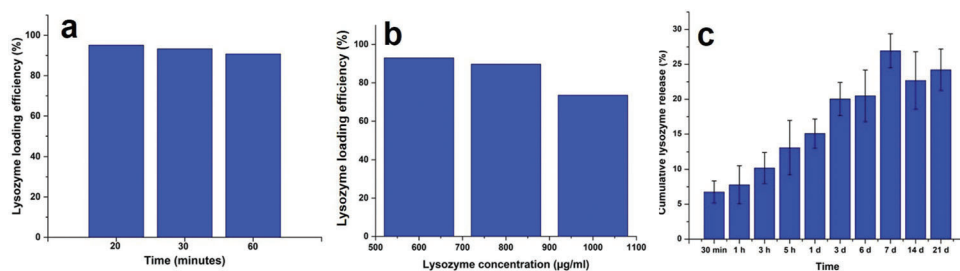


**Figure 3.** Lys loading efficiency versus: a) time (MSNs immersed in a  $1 \text{ mg ml}^{-1}$  Lys solution) and b) concentration (after 20 min immersion), c) Lys release behavior of Ce-MSNs over 21 days at  $37^\circ\text{C}$ .

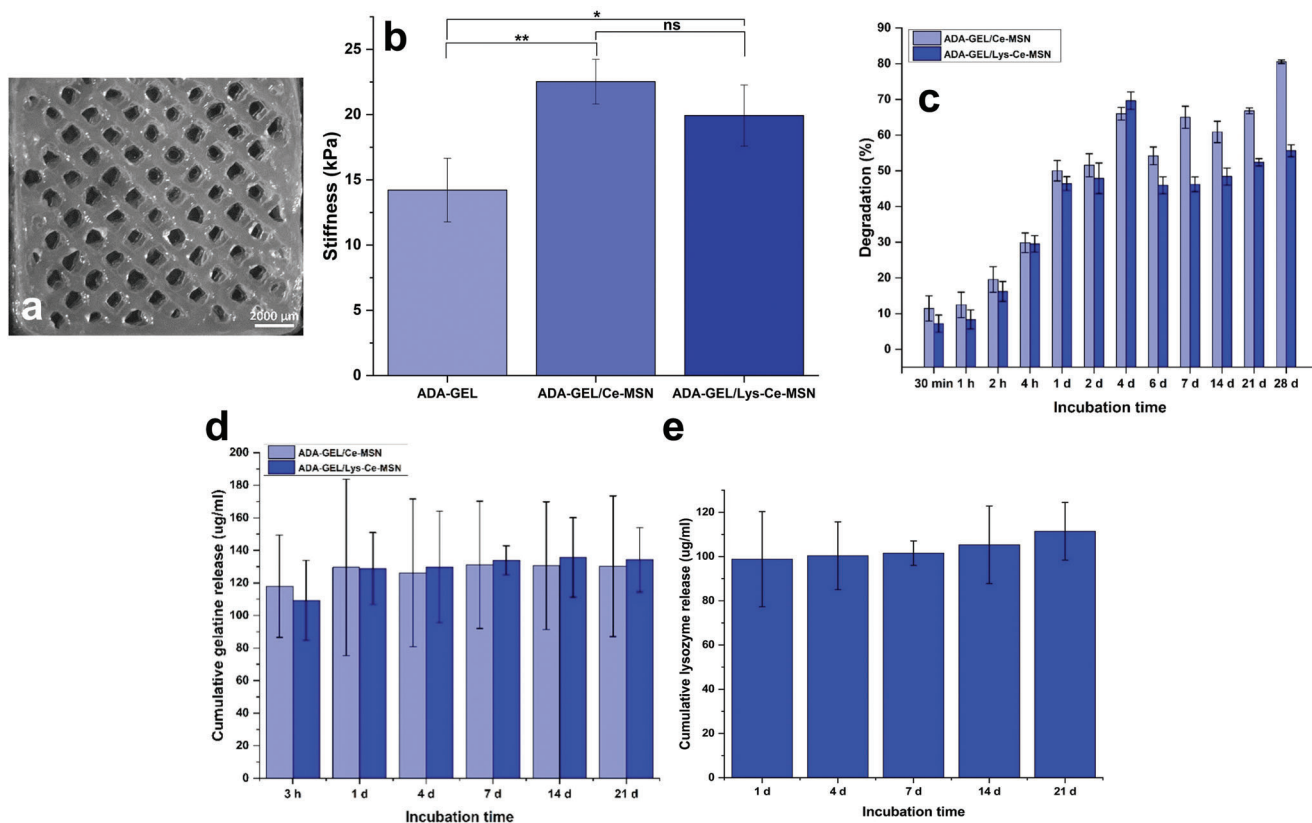


**Figure 4.** a) Stereomicroscopic image showing the 3D printed ADA-GEL/Lys-Ce-MSN scaffold, b) compressive modulus, and c) % degradation of ADA-GEL/Ce-MSN scaffolds with or without Lys, d) GEL, and e) Lys release profile of ADA-GEL/Lys-Ce-MSN scaffolds.

7th day, thereafter some of the unbound Lys molecules re-adsorb on MSNs, reflected in a negligible loss of the amount of the released Lys. In general, the rate of Lys release from Lys-Ce-MSNs was insignificant ( $24 \pm 3\%$  after 21 days), most likely due to robust interaction of the enzyme and MSNs via hydrogen bonding and coordinate bonding.

### 3.3. Physicochemical Properties of ADA-GEL/Ce-MSN Scaffolds

**Figure 4a** shows a stereomicroscopic image of the 3D printed ADA-GEL/Lys-Ce-MSN scaffold whose average pore circularity is  $0.69 \pm 0.05$ , implying proper printing conditions resulting in the formation of quasi-circular pores. Additionally, the 3D printed

scaffold shows an average pore area of  $0.49 \pm 0.82 \text{ mm}^2$  and an average printability of  $1.15 \pm 0.09$ .

The compressive stiffness of the hydrogel nanocomposites with or without Lys compared to that of the neat ADA-GEL scaffold is demonstrated in **Figure 4b**. As seen in this figure, inclusion of Ce-MSNs in ADA-GEL leads to a significant improvement of the compressive stiffness. Such enhancement in mechanical properties originates likely from the emergence of covalent bonds between MSNs and ADA-GEL. Particularly, amine groups of gelatine's amino acids such as lysine or hydroxylysine can chelate Ce cations and form a coordinate bond. The lysine amino acid in gelatine is known to have a single terminal amine on its side chain, that can act as a flexible ligand for chelation of a variety of metal cations. Moreover, the oxygen atom of the

OH group of lysine (that is only available at the C-terminus in a peptide) can dominantly chelate metal cations.<sup>[48]</sup> Another possible strengthening mechanism could be through hydrogen bonding between the amine groups of gelatine and surface hydroxyl groups of the nanoparticles. A comparable behavior has been observed for a hydrogel nanocomposite composed of HA nanoparticle incorporated poly(acrylonitrile-co-1-vinyl imidazole).<sup>[49]</sup> As verified through mechanical testing, Lys does not notably contribute to the improvement of the scaffold's stiffness. This behavior implies that Lys mainly interacts with the nanoparticle carriers rather than with the hydrogel.

### 3.4. Degradation and Enzyme Release Behavior of ADA-GEL/Ce-MSN Scaffolds

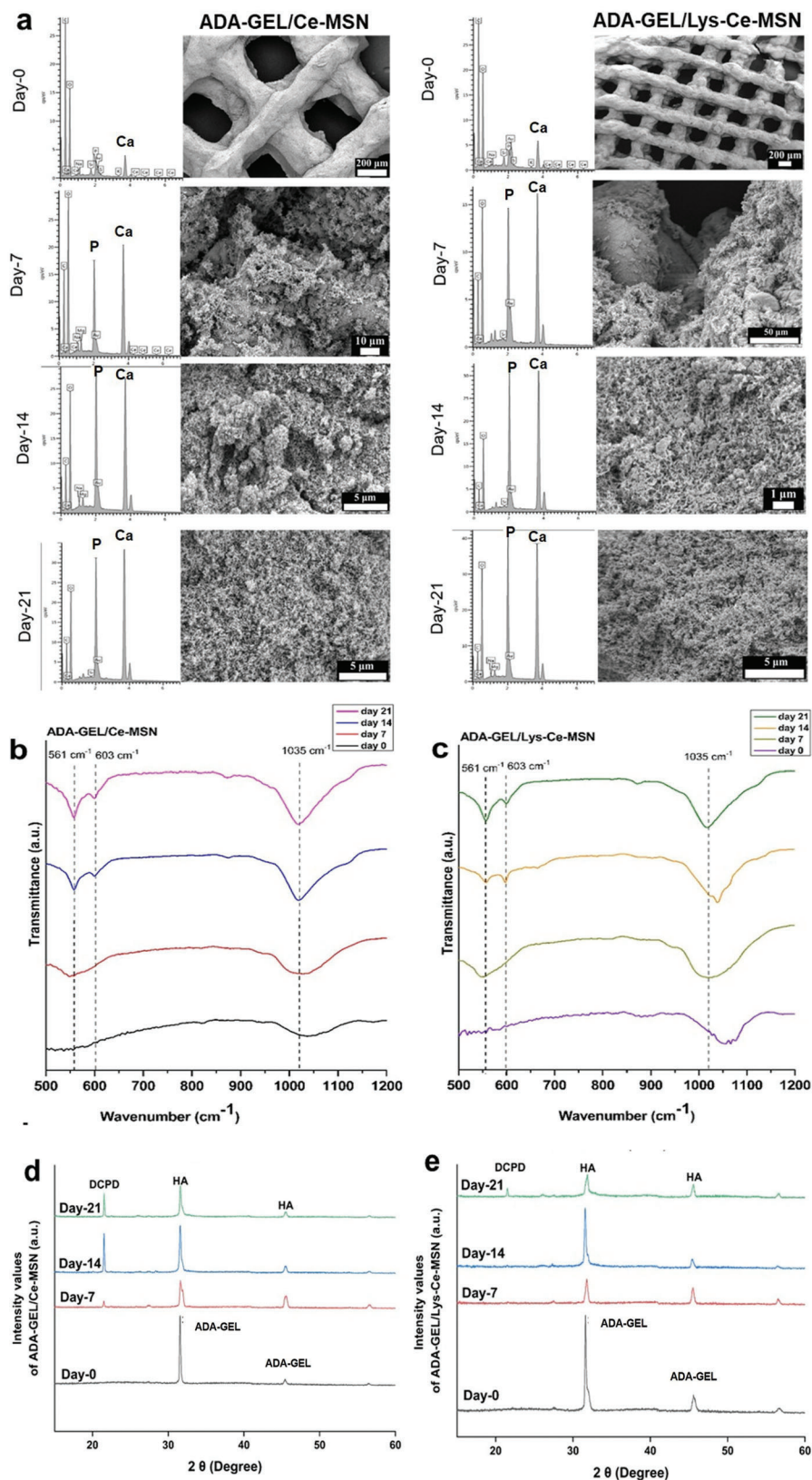
Multifunctional BG/hydrogel scaffolds, including ADA-GEL/Ce-MSN, can address several therapeutic goals such as osteoinductivity and angiogenesis and offer antibacterial, antioxidant, and anticancer effects that are highly demanded for BTE. In the case of inclusion of drug or bioactive agents (e.g., Lys), the hydrogels can also deliver the incorporated cargo in a precise, selective manner. As a result, the scaffolds drive a therapeutic effect at reduced drug dosages by tailoring the delivery to a localized region, thereby excluding concerns related to systemic drug administration and its side effects.<sup>[50,51]</sup> The degradation mode of hydrogel scaffolds dictates the release behavior (kinetics) of the incorporated therapeutic cargo, and thus assessment of degradation in a simulated medium is crucial. Figure 4c shows the in vitro degradation behavior of the ADA-GEL/Ce-MSN scaffolds with or without Lys after immersion in  $\alpha$ -MEM over 28 days. As seen in this graph, both types of hydrogel scaffolds are degraded over time but with a higher rate for those free of Lys. The water (HBSS) induced swelling leads to formation of large voids inside the samples, thereby facilitating further infiltration of water thus intensifying the degradation amount of the scaffolds. Noteworthy, hydrogels made of oxidized alginate typically undergo bulk erosion instead of surface erosion, due to a higher diffusion rate of enzyme or water into the hydrogel bulk compared to the bond scission rate of the hydrogel surface.<sup>[52]</sup> While there is an ascending degradation trend for the ADA-GEL/Ce-MSN scaffolds until day 28, peaked at 78%, the ADA-GEL/Lys-Ce-MSN scaffold reaches a maximum (70%) on the 4th day and thereafter degradation declines (down to 55%). As proven in our recent study,<sup>[3]</sup> MSNs per se act as a cross-linker for ADA-GEL upon bonding of their silanol groups with aldehyde (ADA) and amine or carboxyl groups (glutamic acid or lysine/aspartic acid of GEL), thereby enhancing degradation resistance of the scaffold made thereof. Such covalent bonding between gelatine and silica via their carboxylic acid and silanol groups, respectively, has been previously demonstrated.<sup>[53]</sup> On the other hand, the presence of Lys can further help stabilization of the hydrogel nanocomposite, considering the possibility of peptide-peptide bonding of Lys and GEL and/or hydrogen bonding between the amine and hydroxyl groups of Lys and ADA, respectively. Such intermolecular bonding of enzyme, Ce-MSNs, and ADA-GEL is likely the reason for the improved degradation resistance of ADA-GEL/Lys-Ce-MSN compared to the enzyme-free hydrogel counterpart. Surprisingly, after the 4th day, the ADA-GEL/Lys-Ce-MSN scaffold shows less

degradation tendency that could be due to the release of Lys from Ce-MSNs and their higher exposure to ADA-GEL molecules and thus their further contribution to cross-linking of the polymer chains. Figure 4d shows the GEL release behavior of both hydrogel scaffolds, which does not significantly increase over the course of the incubation time for neither of the scaffolds. This is most likely due to the persistent covalent bonding between the amine groups of GEL's amino acids (lysine or hydroxylysine) and ADA's aldehyde groups. Moreover, given the presence of a high amount of GEL in ADA-GEL, GEL can be subjected to intermolecular renaturation induced by interchain hydrogen bonding.<sup>[54]</sup> As stated by Lazzara et al.<sup>[55]</sup>, a delayed protein (GEL in this study) release can be caused by the protein adsorption in a palisade matrix, leading to a release-resorption-rerelease cycle. Comparing the hydrogel scaffolds with or without Lys, no remarkable discrepancy in terms of GEL release is observed, implying that Lys could have bonded mainly with ADA rather than GEL. Figure 4e demonstrates the cumulative Lys release from the ADA-GEL/Lys-Ce-MSN scaffold over the course of the 21-day immersion time. As seen in this graph, Lys is gradually released from the scaffolds with an insignificant amount. This observation confirms our earlier assumption about the remaining Lys within the hydrogel and its contribution to stabilization (cross-linking) of the scaffold.

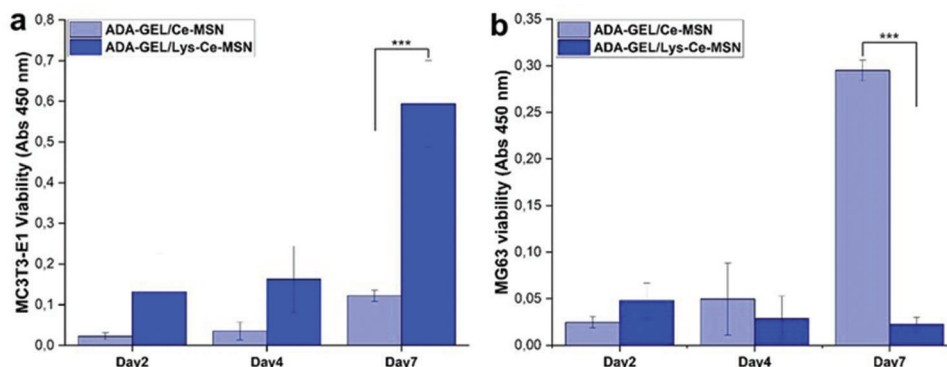
The emergence of a hydroxyapatite (HA) surface layer on hydrogel scaffolds indicates their potential osteoconductivity and bioactivity.<sup>[56]</sup> The evolution of the apatite surface layer was monitored via SEM and surface chemical characterizations such as EDS, XRD analysis, and ATR-FTIR spectroscopy over the course of the immersion of the scaffolds in SBF for up to 21 days.

Figure 5a demonstrates that upon immersion of the nanocomposite scaffolds with or without Lys in SBF, a biomineral surface layer forms that gradually grows over time until day 14 when full coverage of the surface takes place. The elemental composition of the biomineral layer formed after 21-day immersion in SBF, characterized through EDS analysis, verifies the emergence of HA with Ca/P = 1.52 and 1.45 on ADA-GEL/Ce-MSN and ADA-GEL/Lys-Ce-MSN, respectively. The Ca/P  $\approx$  1.52 indicates the emergence of a calcium-deficient HA (CDHA) surface layer on the enzyme-free hydrogel nanocomposites.<sup>[57,58]</sup> Advantageous over stoichiometric HA, CDHA ( $\text{Ca}_{10-x}(\text{PO}_4)_{6-x}(\text{HPO}_4)_x(\text{OH})_{2-x}$ ,  $0 \leq x \leq 1$ ) offers higher biological activity thanks to its composition similarity with biological HA (found in bone, for instance) with Ca/P = 1.5.<sup>[59]</sup> In contrast, the biomineral layer appearing on ADA-GEL/Lys-Ce-MSN is a calcium phosphate compound with further calcium deficiency than CDHA. Comparing the SEM images of the mineralized ADA-GEL/Ce-MSN and mineralized ADA-GEL/Lys-Ce-MSN scaffold, no significant qualitative difference in terms of mineral density is observed. Figures 5b,c show the ATR-FTIR spectra for the mineralized hydrogel nanocomposite scaffolds with or without Lys after their immersion in SBF for given durations. As clearly seen in the spectra, the HA-related doublet dips appearing at 501 and 603  $\text{cm}^{-1}$ , related to O-P-O bending mode,<sup>[60]</sup> emerge upon immersion in SBF, and are intensified over the immersion time. The main broad dip at 1035  $\text{cm}^{-1}$ , which is observed at day 0 (before mineralization) for ADA-GEL/Ce-MSN, is attributed to  $\nu_{\text{asym}}$  (Si-O-Si) bands of  $\text{SiO}_4$  tetrahedra, implying the availability of MSN in this scaffold.<sup>[61,62]</sup>





**Figure 5.** a) EDS spectra and SEM micrographs of ADA-GEL/Ce-MSN (left column) and ADA-GEL/Lys-Ce-MSN (right column) scaffolds over the course of SBF immersion for up to 21 days. ATR-FTIR spectra and XRD patterns for ADA-GEL/Ce-MSN (b and d, respectively) and ADA-GEL/Lys-Ce-MSN (c and e, respectively) scaffolds over the course of SBF immersion.



**Figure 6.** a) MC3T3 cell viability and b) MG63 cell viability for the ADA-GEL/Ce-MSN and ADA-GEL/Lys-Ce-MSN scaffolds after 2, 4, and 7 days incubation (\*\*\* =  $p < 0.001$ ).

In the case of non-mineralized ADA-GEL/Lys-Ce-MSN, this dip slightly shifts to a larger wavenumber, most likely due to the presence of the enzyme and hydrogen bonding between Lys and MSNs. However, upon mineralization of the hydrogel nanocomposites, such broad dips are overlapped by a sharp dip attributed to the P–O stretching vibration mode of HA.<sup>[60]</sup> Figures 5d,e show the XRD patterns of the hydrogel nanocomposites with or without Lys. The characteristic HA peaks that emerge at  $2\theta = 31.5^\circ$  and  $45.5^\circ$  are assigned to (211) and (310) crystal planes, respectively.<sup>[56]</sup> Similarly, these peaks are seen for the hydrogel nanocomposites before mineralization, implying that ADA-GEL can also show such crystallographic planes, as previously reported by Sarker et al.<sup>[16]</sup> However, as soon as the hydrogel nanocomposite surface is mineralized, the peaks intensity declines, implying that less crystalline HA covers the surface. There is an extra peak at  $2\theta = 21^\circ$  that appears after mineralization of ADA-GEL/Ce-MSN. As reported by Harding and Krebs,<sup>[56]</sup> this peak does not correlate with the formation of apatite and can be associated to dicalcium phosphate dihydrate (DCPD). Under physiological conditions, such a metastable calcium phosphate polymorph can transform to apatite, as reflected by the appearance of the HA peaks mentioned above.<sup>[63]</sup> Noteworthy, Lys incorporated in the hydrogel nanocomposite inhibited the formation of DCPD, most likely due to highly positively charged moieties at SBF's pH, which affect the nucleation and growth of this calcium phosphate polymorph.

As discussed earlier, the hydrogel scaffolds with or without Lys can induce the creation of a surface apatite layer that indicates bioactivity and osteoconductivity of the developed materials. To validate the latter feature, interactions of pre-osteoblast (MC3T3-E1) cells and the hydrogel nanocomposite scaffolds were monitored. As shown in **Figure 6a**, with regards to the viability of MC3T3-E1 cells, during the incubation period of cell-hydrogel nanocomposite, i.e., 7 days, the cell number increased, particularly with a higher rate for the hydrogel nanocomposites containing Lys. The supportive effect of Lys on proliferation of MC3T3-E1 cells, particularly after 7 days, can be associated to its stabilizing contribution to the hydrogel structure, reflected in a less degradation level, as previously shown in **Figure 4c**. The enzyme free hydrogel nanocomposite is more vulnerable to degradation and thus releases a larger amount of  $\text{Ca}^{2+}$  and thereby alkalizes the medium. Within the alkaline medium, the viability of MC3T3-

E1 cells declines and the cells do not differentiate to a large extent in comparison to the cells adjacent to the other scaffold type. Additionally, thanks to the presence of amide groups, Lys can chelate  $\text{Ca}^{2+}$  ions and thereby neutralize their negative effect on cell viability. In contrast to its positive impact on MC3T3-E1 (normal) cell viability, Lys has a negative effect on the proliferation of MG63 osteosarcoma cells, **Figure 6b**. ADA-GEL has been shown to have a non-harmful effect on MG63 cells,<sup>[22]</sup> therefore less viability of these cells adjacent to the nanocomposite hydrogel scaffold can solely be attributed to Lys. It is worthy to note that MG63 osteosarcoma cells have been considered as a cancer cell model to monitor the anticancer properties of different compounds such as quinoline-platinum complex,<sup>[64]</sup> doxorubicin hydrochloride,<sup>[65]</sup> lactoferrin,<sup>[66]</sup> among others. Anticancer effects of Lys have been proven by other research groups and have been attributed to the increased production of reactive oxygen species (ROS) by this enzyme.<sup>[67]</sup> MG63 cells are already subjected to oxidative stress, owing to a high concentration of internal ROS and downregulation of antioxidant factors.<sup>[68,69]</sup> As a result, these cells can be harmed by extra ROS generation to a larger extent than normal cells. Somu and Paul<sup>[67]</sup> state that ROS generation is mainly responsible for cancer cell death, while negligibly damages healthy cells.

Cell morphology (shape) and cell distribution mode were observed by staining the cells with Calcein/DAPI and Phalloidin/DAPI and cell imaging by fluorescence microscopy, **Figure 7**. The Calcein/DAPI and Phalloidin/DAPI images implied an inferior density of MG63 cells on both hydrogel nanocomposite scaffolds with or without Lys. In contrast, normal cells (MC3T3-E1) are abundant on the hydrogel nanocomposites' surface. It is worthy to note that some part of the colored (both red and green) spots can be attributed to MSNs rather than the cells due to their mesoporous structure providing a high binding capacity.<sup>[70]</sup> However, considering the low concentration of MSNs in our study (0.1% (w/v)), this interference could be negligible, as compared to that reported by Guduric et al.,<sup>[70]</sup> i.e., 7 wt.%. The population of MC3T3-E1 cells on the scaffold's surface rose over time and peaked at day 7. Comparing the cell density on the hydrogel nanocomposites with or without Lys, it is obvious that Lys has played a major role and further supported adhesion and proliferation of the MC3T3-E1 cells. This behavior might originate from Lys' stabilizing/reinforcing effect for the hydrogel scaffolds,

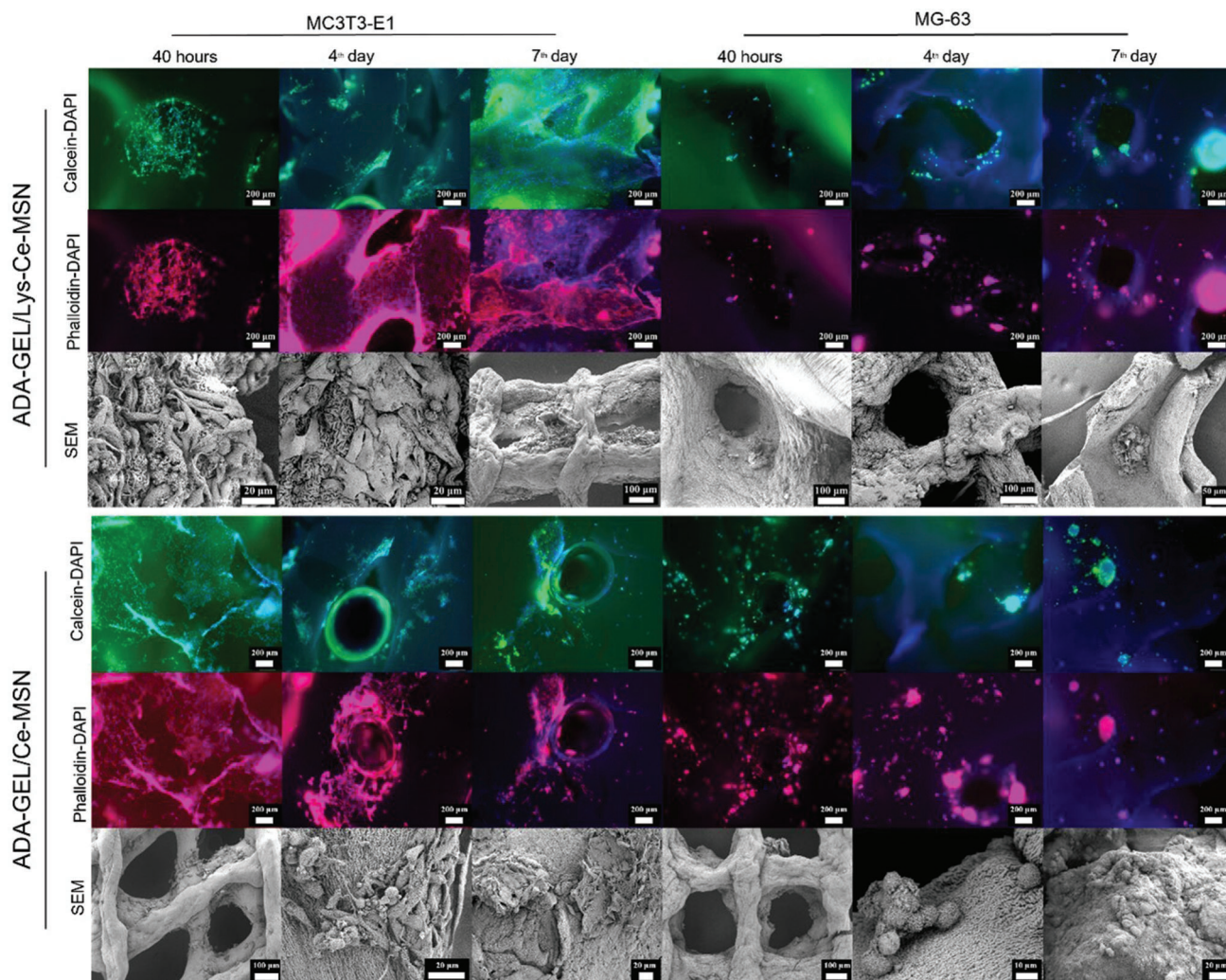


**Figure 7.** Morphology of MC3T3-E1 and MG63 cells adhered on ADA-GEL/Ce-MSN and ADA-GEL/Lys-Ce-MSN scaffolds imaged by fluorescence microscopy (after Calcein/DAPI and Phalloidin/DAPI staining) and SEM i after 40 h, 4 days, and 7 days incubation.

lowering their degradation rate. On the other hand, thanks to large ROS generation, Lys has offered an antiproliferative effect and inhibited the surface accumulation of the osteosarcoma cells. SEM micrographs clearly show that normal cells are stretched and expanded largely on the surface of the hydrogel scaffolds with or without Lys. In contrast, the osteosarcoma cells are either rarely adhered to the Lys-containing scaffolds or are seen as round, individual cells scattered on the Lys-free scaffold's surface. Conclusively, both hydrogel nanocomposite scaffolds properly allow for adhesion and growth of MC3T3-E1 cells, while discouraging the cellular activity of MG63 cells, particularly when Lys is available within the scaffold. The adhesion mode of MC3T3-E1 cells on both hydrogel nanocomposite scaffolds, i.e., widespread of the cells and formation of actin filaments, indicates the beginning of osteoblast differentiation, without application of osteogenic driving factors.<sup>[71]</sup>

In addition to mechanical stiffness and composition, as two influential factors dictating cell-material interactions, surface topography, and surface charge are also decisive. ADA-GEL surface

is negatively charged thanks to the abundance of carboxyl and hydroxyl groups. On the other hand, possessing silanol groups, MSNs are also negatively charged. Considering the negative charge of the cell membrane,<sup>[72]</sup> the cells could be repelled electrostatically from the ADA-GEL/Ce-MSN surface. However, the presence of Lys and particularly GEL with the positively charged (protonated) amine functional moieties can lower this repulsion allowing cells to adhere to specific regions of the surface that are electrostatically favorable. Last, living cells' shape and adhesion mode depend on the local nanoscale topography.<sup>[73]</sup> The availability of Ce-MSNs raises surface roughness and reduces porosity, owing to the interaction of the nanoparticles with ADA-GEL via intermolecular bonding. As a result, a dense surface with rough nanotopography can be created that provokes cell attachment. This is reflected in the morphology of the MC3T3-E1 cells adhered to both hydrogel nanocomposites indicating that cells are available in a large number and are flattened on an extensive area.

The specific ALP activity and mineralization (formation of HA crystals) by MC3T3-E1 cells were quantified to evaluate the os-

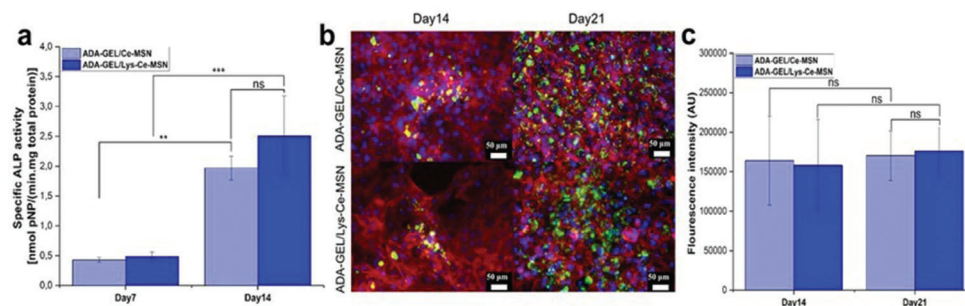


**Figure 8.** a) Specific ALP activity of the differentiating MC3T3-E1 cells (\*\*\*:  $p < 0.001$ , \*\*:  $p < 0.01$ , ns: non-significant), b) phalloidin/DAPI staining of the MC3T3-E1 cells adhered on the hydrogel nanocomposite scaffolds' surface with or without Lys after 14 and 21 days incubation. The green-colored phase represents the cell-induced biom mineralization of the scaffold surface (the scale bars represent 50  $\mu\text{m}$ ). c) Cell-induced mineralization on the hydrogel nanocomposite scaffolds represented by fluorescence intensity after 14 and 21 days incubation.

teogenic differentiation capacity of the cells seeded on the hydrogel nanocomposite scaffolds. As seen in **Figure 8a**, compared to day 7, both scaffolds induce a significantly increased ALP activity ( $p < 0.01$  and  $< 0.001$  for ADA-GEL/Ce-MSN and ADA-GEL/Lys-Ce-MSN, respectively), indicating a favorable osteogenesis capability. Among the hydrogel scaffolds, ADA-GEL/Lys-Ce-MSN offered a lower differentiating performance, most likely due to its

higher resistance against degradation and thus GEL release that provokes osteogenic differentiation.<sup>[3]</sup> Such a behavior was similarly observed in our earlier study, where icariin could stabilize the structure of ADA-GEL and thus hamper GEL release.<sup>[34]</sup> **Figure 8b** shows phalloidin/DAPI images that visualize cell-induced mineralization adjacent to the hydrogel nanocomposites after 14- and 21 days incubation. In general, the ions released from

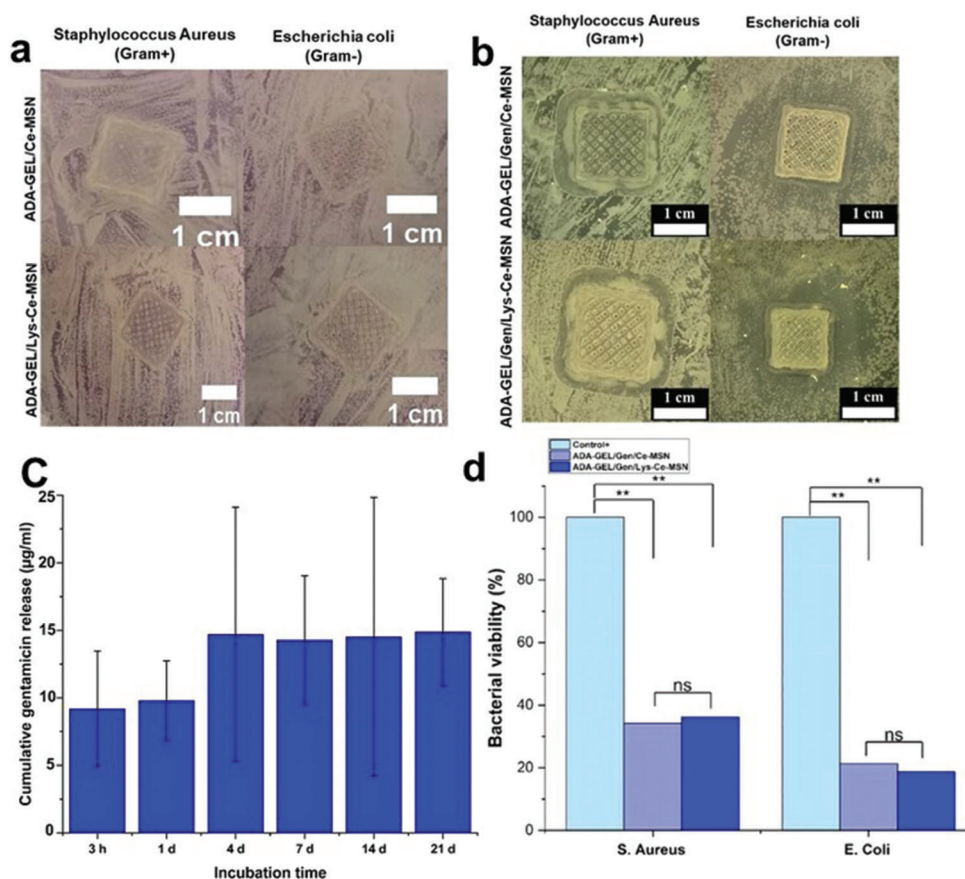


**Figure 9.** Antibacterial activities of the hydrogel nanocomposite scaffolds with or without Lys: a) and b) camera images showing the formation of an inhibition zone around the scaffolds, c) gentamicin release behavior of ADA-GEL/Gen/Lys-Ce-MSN scaffolds over 21 days incubation, d) bacterial viability (quantified via turbidity assay) adjacent to the hydrogel nanocomposite scaffolds (\*\*:  $p < 0.01$ , ns: non-significant).

MSNs into body fluid promote the formation of hydroxyl carbonate apatite (HCA) and excite the genes that contribute to osteogenesis.<sup>[74]</sup> After 21 days of cell culture, the Lys containing hydrogel nanocomposite appeared to be slightly more encouraging toward apatite formation than the enzyme-free nanocomposite. This observation was confirmed quantitatively, as shown in Figure 8c. Such a discrepancy in apatite mineralization could be associated with the larger population of cells in a medium containing Lys. As discussed earlier (Figure 6a), the MC3T3-E1 cells proliferate more in a less alkaline medium, created in the presence of Lys that can chelate Ca<sup>2+</sup> ions.

Lys is an enzyme well-known for its antibacterial activity via hydrolysis of the cell walls of bacteria.<sup>[75]</sup> However, as seen in Figure 9a, where antibacterial activity of the ADA-GEL/Lys-Ce-MSN scaffold is demonstrated, the potential of Lys loaded on Ce-MSNs and entrapped within ADA-GEL for inactivation of bacteria is negligible and should be augmented by supplementary antibacterial drugs. In this study, we coupled Lys with Gen to develop a broad-spectrum antibacterial hydrogel scaffold. Figure 9b shows the bacterial inhibition zone formed around the 3D printed ADA-GEL/Gen/Ce-MSN scaffolds with or without Lys. Irrespective of the bacteria type, the hydrogel scaffold releasing Lys shows a recognizable bacteria-free boundary that is more evident than that for the scaffolds without Lys and incorporating only Gen. This might originate from the Gen release, leading to the availability of a less significant amount of Gen compared to Lys (Figure 9c vs. Figure 4e). Despite such an observation, the quantified antibacterial efficiency (via turbidity assay), Figure 9d, indicates no significant discrepancy between the hydrogel scaffolds with or without Lys. The bactericidal mechanism of Lys is attributed to its catalytic role in the hydrolysis of 1,4- $\beta$  linkages between N-acetyl-D-glucosamine and N-acetylmuramic acid in the cell wall of bacteria.<sup>[76]</sup> Noteworthy, Lys has been proven to be more functional against gram-positive bacteria (e.g., *S. aureus*)<sup>[47,77]</sup> than gram-negative bacteria (e.g., *E. coli*), for which the lipopolysaccharide layer covering their outmost membrane hampers Lys infiltration.<sup>[78]</sup> However, ADA-GEL/Gen/Lys-Ce-MSN scaffold did not show superior antibacterial performance when exposed to gram-positive bacteria, most likely due to partial contribution of Gen and its release, leading to the inactivation of both gram-positive and gram-negative bacteria equally.

#### 4. Conclusions

The incorporation of Lys-Ce-MSNs in ADA-GEL and 3D printing of the as-developed nanocomposite hydrogel enabled the creation of customizable, multifunctional scaffolds for bone tissue engineering. The nanofiller provides an outstanding platform assuring bioactivity, witnessed by large, rapid formation of a calcium phosphate phase on the scaffold surface in SBF, and proper cell-material interactions. Additionally, the added Ce-MSNs allow for co-delivery of beneficial ions for bone regeneration as well as biological agents such as Lys that offer anticancer and antibacterial properties. Lys could also raise the mechanical stability and degradation resistance of the hydrogel scaffolds, thereby indirectly affecting osteoblast cell behavior. While pre-osteoblast cells were shown to have improved proliferation and adhesion on the scaffolds due to the release of Lys, osteosarcoma cells were less vi-

able. This selective cytotoxicity is crucial for possible anticancer applications. Lys is recognized for its antibacterial activity, particularly against gram-positive bacteria. However, in the current study, the presence or absence of Lys did not contribute largely to the antibacterial property of the scaffolds. This effect might originate from the minor concentration of included Lys. Therefore, the biological effects of the enzyme dosage as loaded on MSNs or simply distributed in the hydrogel scaffold should be further evaluated in future work. Moreover, the cross talk between osteoblasts and osteoclasts and its influence on bone remodelling in the presence of the hydrogel nanocomposites should be studied.

#### Acknowledgements

Useful discussions with Dr. R. Detsch (Institute of Biomaterials, FAU) are appreciated.

Open Access funding enabled and organized by Projekt DEAL.

#### Conflict of Interest

The authors declare no conflict of interest.

#### Authors Contribution

M.M. performed investigation, validation, formal analysis, and wrote the original draft. R.M. performed investigation and reviewed & edited the final manuscript. S.H. performed formal analysis, wrote the original draft, and reviewed & edited the final manuscript. M.F.-C. performed methodology, validation, supervision, and reviewed & edited the final manuscript. Q.N. performed investigation and reviewed & edited the final manuscript. Me.Mo. performed formal analysis and reviewed & edited the final manuscript. A.R.B. provided resources, conceptualization, formal analysis, supervision, and reviewed & edited the final manuscript.

#### Data Availability Statement

The data that support the findings of this study are available from the corresponding author upon reasonable request.

#### Keywords

3D printing, bone tissue engineering, drug delivery, lysozyme, mesoporous SiO<sub>2</sub>-CaO nanoparticles

Received: March 16, 2022

Revised: May 12, 2022

Published online: July 19, 2022

- [1] X. Zhai, Y. Ma, C. Hou, F. Gao, Y. Zhang, C. Ruan, H. Pan, W. W. Lu, W. Liu, *ACS Biomater. Sci. Eng.* **2017**, *3*, 1109.
- [2] S. S. Homaeigohar, M. Shokrgozar, J. Javadpour, A. Khavandi, A. Y. Sadi, *J. Biomed. Mater. Res.* **2006**, *78*, 129.
- [3] M. Monavari, S. Homaeigohar, M. Fuentes-Chandía, Q. Nawaz, M. Monavari, A. Venkatraman, A. R. Boccaccini, *Mater. Sci. Eng. C* **2021**, *131*, 112470.

- [4] P. Gupta, M. Adhikary, M. Kumar, N. Bhardwaj, B. B. Mandal, *ACS Appl. Mater. Interfaces* **2016**, *8*, 30797.
- [5] X. - F. Wang, Y. Song, Y. - S. Liu, Y.u-C. Sun, Y.u-G. Wang, Y. Wang, P. - J. Lyu, *PLoS One* **2016**, *11*, e0157214.
- [6] M. Guvendiren, J. Molde, R. M. Soares, J. Kohn, *ACS Biomater. Sci. Eng.* **2016**, *2*, 1679.
- [7] D. Tang, R. S. Tare, L.-Y.o Yang, D. F. Williams, K. - L. Ou, R. O. C. Oreffo, *Biomaterials* **2016**, *83*, 363.
- [8] Á. J. Leite, B. Sarker, T. Zehnder, R. Silva, J. F. Mano, A. R. Boccaccini, *Biofabrication* **2016**, *8*, 035005.
- [9] U. Rottensteiner, B. Sarker, D. Heusinger, D. Dafinova, S. Rath, J. Beier, U. Kneser, R. Horch, R. Detsch, A. Boccaccini, A. Arkudas, *Materials* **2014**, *7*, 1957.
- [10] Y. Zhu, Z. Ma, L. Kong, Y. He, H. F. Chan, H. Li, *Biomaterials* **2020**, *256*, 120216.
- [11] Z. Yang, F. Zhao, W. Zhang, Z. Yang, M. Luo, Lu Liu, X. Cao, D. Chen, X. Chen, *Chem. Eng. J.* **2021**, *419*, 129520.
- [12] T. Jungst, W. Smolan, K. Schacht, T. Scheibel, J. Groll, *Chem. Rev.* **2016**, *116*, 1496.
- [13] K. Y. Lee, D. J. Mooney, *Prog. Polym. Sci.* **2012**, *37*, 106.
- [14] S. N. Pawar, K. J. Edgar, *Biomaterials* **2012**, *33*, 3279.
- [15] S. Homaeigohar, A. R. Boccaccini, *Acta Biomater.* **2020**, *107*, 25.
- [16] B. Sarker, D. G. Papageorgiou, R. Silva, T. Zehnder, F. Gul-E-Noor, M. Bertmer, J. Kaschta, K. Chrissafis, R. Detsch, A. R. Boccaccini, *J. Mater. Chem. B* **2014**, *2*, 1470.
- [17] D. Biswal, B. Anupriya, K. Uvanesh, A. Anis, I. Banerjee, K. Pal, *J. Mech. Behav. Biomed. Mater.* **2016**, *53*, 174.
- [18] S. Homaeigohar, T.-Y.u Tsai, T. - H. Young, H. J.u Yang, Y. - R. Ji, *Carbohydr. Polym.* **2019**, *224*, 115112.
- [19] J. A. Rowley, G. Madlambayan, D. J. Mooney, *Biomaterials* **1999**, *20*, 45.
- [20] F. Ruther, T. Distler, A. R. Boccaccini, R. Detsch, *J. Mater. Sci.: Mater. Med.* **2018**, *30*, 8.
- [21] B. Sarker, R. Singh, R. Silva, J. A. Roether, J. Kaschta, R. Detsch, D. W. Schubert, I. Cicha, A. R. Boccaccini, *PLoS One* **2014**, *9*, e107952.
- [22] T. Zehnder, B. Sarker, A. R. Boccaccini, R. Detsch, *Biofabrication* **2015**, *7*, 025001.
- [23] V. Bednarzig, E. Karakaya, A. L. Egaña, J. Teřmar, A. R. Boccaccini, R. Detsch, *Bioprinting* **2021**, *23*, e00145.
- [24] B. Sarker, W. Li, K. Zheng, R. Detsch, A. R. Boccaccini, *ACS Biomater. Sci. Eng.* **2016**, *2*, 2240.
- [25] T. - H. Kim, R. K. Singh, M. S. Kang, J. - H. Kim, H. - W. Kim, *Nanoscale* **2016**, *8*, 8300.
- [26] A. Bari, N. Bloise, S. Fiorilli, G. Novajra, M. Vallet-Regí, G. Bruni, A. Torres-Pardo, J. M. González-Calbet, L. Visai, C. Vitale-Brovarone, *Acta Biomater.* **2017**, *55*, 493.
- [27] A. El-Fiqi, T. - H. Kim, M. Kim, M. Eltohamy, J. - E. Won, E. - J. Lee, H. - W. Kim, *Nanoscale* **2012**, *4*, 7475.
- [28] K. Zheng, E. Torre, A. Bari, N. Taccardi, C. Cassinelli, M. Morra, S. Fiorilli, C. Vitale-Brovarone, G. Iviglia, A. R. Boccaccini, *Materials Today Bio* **2020**, *5*, 100041.
- [29] A. Pellegrini, U. Thomas, N. Bramaz, S. Klausner, P. Hunziker, R. Von Fellenberg, *J. Appl. Microbiol.* **1997**, *82*, 372.
- [30] J. Kovacs-Nolan, M. Phillips, Y. Mine, *J. Agric. Food Chem.* **2005**, *53*, 8421.
- [31] B. S. Vasile, O. Oprea, G. Voicu, A. Ficai, E. Andronescu, A. Teodorescu, A. Holban, *Int. J. Pharm.* **2014**, *463*, 161.
- [32] B. J. Chaves, P. Tadi, *Gentamicin*, StatPearls Publishing, Treasure Island (FL) **2021**.
- [33] S. A. Ragland, A. K. Criss, *PLoS Pathog.* **2017**, *13*, e1006512.
- [34] C. Li, H. Chen, B. Chen, G. Zhao, *Crit. Rev. Food Sci. Nutr.* **2018**, *58*, 689.
- [35] Q. Liang, Q. Hu, G. Miao, B.o Yuan, X. Chen, *Mater. Lett.* **2015**, *148*, 45.
- [36] D. Kozon, K. Zheng, E. Boccardi, Y. Liu, L. Liverani, A. Boccaccini, *Materials* **2016**, *9*, 225.
- [37] K. Zheng, P. Balasubramanian, T. E. Paterson, R. Stein, S. MacNeil, S. Fiorilli, C. Vitale-Brovarone, J. Shepherd, A. R. Boccaccini, *Mater. Sci. Eng. C* **2019**, *103*, 109764.
- [38] L. Ouyang, R. Yao, Y.u Zhao, W. Sun, *Biofabrication* **2016**, *8*, 035020.
- [39] T. Kokubo, H. Takadama, *Biomaterials* **2006**, *27*, 2907.
- [40] Y. Andriani, H. Mohamad, K. Bhubalan, M. I. Abdullah, H. Amir, *J. Sustainability Sci. Manage.* **2017**, *12*, 45.
- [41] K. Zheng, A. Solodovnyk, W. Li, O. - M. Goudouri, C. Stähli, S. N. Nazhat, A. R. Boccaccini, *J. Am. Ceram. Soc.* **2015**, *98*, 30.
- [42] M. S. Bhattacharyya, P. Hiwale, M. Piras, L. Medda, D. Steri, M. Piludu, A. Salis, M. Monduzzi, *J. Phys. Chem. C* **2010**, *114*, 19928.
- [43] S. Xu, Y. Liu, Y. Yu, X. Zhang, J. Zhang, Y. Li, *Sep. Purif. Technol.* **2020**, *235*, 116185.
- [44] K. Zheng, N. Taccardi, A. M. Beltrán, B. Sui, T. Zhou, V. R. R. Marthala, M. Hartmann, A. R. Boccaccini, *RSC Adv.* **2016**, *6*, 95101.
- [45] V. A. Proctor, F. Cunningham, D. Y. Fung, *Crit. Rev. Food Sci. Nutr.* **1988**, *26*, 359.
- [46] R. Luo, X. Zhou, Yi Xiu, H. Wang, *J. Sol-Gel Sci. Technol.* **2018**, *87*, 584.
- [47] K. Zheng, M. Lu, Y. Liu, Q. Chen, N. Taccardi, N. Hüser, A. R. Boccaccini, *Biomed. Mater.* **2016**, *11*, 035012.
- [48] A. A. Clark, B.o Yang, M. T. Rodgers, P. B. Armentrout, *J. Phys. Chem. B* **2019**, *123*, 1983.
- [49] B. Xu, P. Zheng, F. Gao, W. Wang, H. Zhang, X. Zhang, X. Feng, W. Liu, *Adv. Funct. Mater.* **2017**, *27*, 1604327.
- [50] A. Dash, G. Cudworth II, *J. Pharmacol. Toxicol. Methods* **1998**, *40*, 1.
- [51] S. Stewart, J. Domínguez-Robles, V. Mcilorum, E. Mancuso, D. Lamprou, R. Donnelly, E. Larrañeta, *Pharmaceutics* **2020**, *12*, 105.
- [52] T. Boonthekul, H. - J. Kong, D. J. Mooney, *Biomaterials* **2005**, *26*, 2455.
- [53] L. S. Connell, L. Gabrielli, O. Mahony, L. Russo, L. Cipolla, J. R. Jones, *Polym. Chem.* **2017**, *8*, 1095.
- [54] J. L. Gornall, E. M. Terentjev, *Soft Matter* **2008**, *4*, 544.
- [55] T. D. Lazzara, I. Mey, C. Steinem, A. Janshoff, *Anal. Chem.* **2011**, *83*, 5624.
- [56] J. L. Harding, M. D. Krebs, *Macromol. Mater. Eng.* **2016**, *301*, 1172.
- [57] F. C. M. Driessens, M. G. Boltong, E. A. P. De Maeyer, R. Wenz, B. Nies, J. A. Planell, *Biomaterials* **2002**, *23*, 4011.
- [58] S. Homaeigohar, T.-Y.u Tsai, E. S. Zarie, M. Elbahri, T. - H. Young, A. R. Boccaccini, *Mater. Sci. Eng., C* **2020**, *116*, 111248.
- [59] H. Begam, B. Kundu, A. Chanda, S. K. Nandi, *Ceram. Int.* **2017**, *43*, 3752.
- [60] X. L. Tang, X. F. Xiao, R. F. Liu, *Mater. Lett.* **2005**, *59*, 3841.
- [61] M. Cerruti, D. Greenspan, K. Powers, *Biomaterials* **2005**, *26*, 1665.
- [62] M. Mačković, A. Hoppe, R. Detsch, D. Mohn, W. J. Stark, E. Spiecker, A. Boccaccini, *J. Nanopart. Res.* **2012**, *14*, 966.
- [63] M. Iijima, H. Kamemizu, N. Wakamatsu, T. Goto, Y. Doi, Y. Moriwaki, *J. Cryst. Growth* **1997**, *181*, 70.
- [64] M. C. Ruiz, A. Resasco, A. L. Di Virgilio, M. Ayala, I. Cavaco, S. Cabrera, J. Aleman, I. E. León, *Cancer Chemother. Pharmacol.* **2019**, *83*, 681.
- [65] D. Das, A. P. Rameshbabu, P. Ghosh, P. Patra, S. Dhara, S. Pal, *Carbohydr. Polym.* **2017**, *171*, 27.
- [66] J. P. Guedes, C. S. Pereira, L. R. Rodrigues, M. Côrte-Real, *Front. Oncol.* **2018**, *8*, 200.
- [67] P. Somu, S. Paul, *Colloids Surf., B* **2019**, *178*, 297.
- [68] W. Mu, L. - Z. Liu, *React. Oxygen Species* **2017**, *4*, 251.
- [69] A. J. Montero, J. Jasse, *Drugs* **2011**, *71*, 1385.
- [70] V. Guduric, J. Wieckhusen, A. Bernhardt, T. Ahlfeld, A. Lode, C. Wu, M. Gelinsky, Composite Bioinks With Mesoporous Bioactive Glasses— A Critical Evaluation of Results Obtained by, **2022**.
- [71] D. Hong, H. - X. Chen, H. - Q. Yu, Y. Liang, C. Wang, Q. - Q. Lian, H. - T. Deng, R. - S. Ge, *Exp. Cell Res.* **2010**, *316*, 2291.

- [72] C. J. Wilson, R. E. Clegg, D. I. Leavesley, M. J. Percy, *Tissue Eng.* **2005**, *11*, 1.
- [73] T. Dvir, B. P. Timko, D. S. Kohane, R. Langer, *Nat. Nanotechnol.* **2011**, *6*, 13.
- [74] X. Shen, P. Yu, H. Chen, J. Wang, B. Lu, X. Cai, C. Gu, G. Liang, D. Hao, Q. Ma, Y. Li, *RSC Adv.* **2020**, *10*, 12105.
- [75] P. Zhuang, K. Li, K. Qian, D. Li, X. Mei, *IET Nanobiotechnol.* **2020**, *14*, 412.
- [76] K. Deshmukh, Y. S. Tanwar, S. Sharma, P. Shende, R. Cavalli, *Biomed. Pharmacother.* **2016**, *84*, 485.
- [77] B. Masschalck, C. W. Michiels, *Crit. Rev. Microbiol.* **2003**, *29*, 191.
- [78] L. França De Oliveira, K. De Almeida Gonçalves, F. H. Boreli, J. Kobarg, M. B. Cardoso, *J. Mater. Chem.* **2012**, *22*, 22851.